Single-Channel sEMG-Based Estimation of Knee Joint Angle Using a Decomposition Algorithm With a State-Space Model

Song Zhang, Ningbo Yu, *Member, IEEE*, Zhenhui Guo, Weiguang Huo, and Jianda Han, *Member, IEEE*

***Abstract*— Accurate human motion estimation is crucial for effective and safe human-robot interaction when using robotic devices for rehabilitation or performance enhancement. Although surface electromyography (sEMG) signals have been widely used to estimate human movements, conventional sEMG-based methods, which need sEMG signals measured from multiple relevant muscles, are usually subject to some limitations, including interference between sEMG sensors and wearable robots/environment, complicated calibration, as well as discomfort during long-term routine use. Few methods have been proposed to deal with these limitations by using single-channel sEMG (i.e., reducing the sEMG sensors as much as possible). The main challenge for developing single-channel sEMG-based estimation methods is that high estimation accuracy is difficult to be guaranteed. To address this problem, we proposed an sEMG-driven state-space model combined with an sEMG decomposition algorithm to improve the accuracy of knee joint movement estimation based on single-channel sEMG signals measured from gastrocnemius. The effectiveness of the method was evaluated via both single- and multi-speed walking experiments with seven and four healthy subjects, respectively. The results showed that the normal root-mean-squared error of the estimated knee joint angle using the method could be limited to 15%. Moreover, this method is robust with respect to variations in walking speeds. The estimation performance of this method was basically comparable to that of state-of-the-art studies using multi-channel sEMG.**

***Index Terms*— Single-channel sEMG, joint movement estimation, decomposition, state-space model.**

Manuscript received 14 April 2023; revised 12 October 2023; accepted 17 November 2023. Date of publication 28 November 2023; date of current version 4 December 2023. This work was supported in part by the National Key Research and Development Program of China under Grant 2022YFB4700203, in part by the National Natural Science Foundation of China under Grant U1913208, and in part by the Science and Technology Program of Tianjin under Grant 21JCZDJC00170. *(Corresponding author: Weiguang Huo.)*

This work involved human subjects or animals in its research. Approval of all ethical and experimental procedures and protocols was granted by the Local Ethics Committee of Nankai University, Tianjin, China.

Song Zhang is with the School of Physics and Electronic Information, Anhui Normal University, Wuhu 241002, China, and also with the College of Artificial Intelligence and the Tianjin Key Laboratory of Intelligent Robotics, Nankai University, Tianjin 300350, China (e-mail: s.zhang@ahnu.edu.cn).

Ningbo Yu, Weiguang Huo, and Jianda Han are with the College of Artificial Intelligence and the Tianjin Key Laboratory of Intelligent Robotics, Nankai University, Tianjin 300350, China, and also with the Institute of Intelligence Technology and Robotic Systems, Shenzhen Research Institute, Nankai University, Shenzhen 518083, China (e-mail: nyu@nankai.edu.cn; weiguang.huo@nankai.edu.cn; hanjianda@nankai.edu.cn).

Zhenhui Guo is with the College of Artificial Intelligence and the Tianjin Key Laboratory of Intelligent Robotics, Nankai University, Tianjin 300350, China (e-mail: 2120210415@mail.nankai.edu.cn).

Digital Object Identifier 10.1109/TNSRE.2023.3336317

I. Introduction

IN CHINA, the number of patients suffering from stroke was 13.00 million in 2019 [1]. Many stroke survivors suffer from knee impairments, which makes walking difficult or even impossible [2]. Knee exoskeletons can provide extension assistance for these patients to perform daily life activities, such as walking and standing [3], [4]. Most of these devices face the challenge of how to ensure accurate and safe human-robot interaction (HRI) [5]. To improve the HRI, bioelectric signals, such as electromyogram and electroencephalogram [6], or electrical impedance tomography signals [7], have been used for controlling the robotic devices. Surface electromyography (sEMG) signal has been widely used as an effective means for estimating human state/intention in HRI due to its characteristics such as non-invasive application, accurate measurement of muscle activity, and the capability of predicting human motion (i.e., preceding the corresponding motion by 20-100 ms) [8], [9], [10].

For sEMG-based HRI, an important issue is to decode human movement intention, including discrete and continuous movements. The continuous movements, such as joint angles, joint moments, and angular velocities, can make the robotic devices consistent with human movement. Many approaches have been proposed to estimate continuous human joint movements based on sEMG signals, such as BP neural network [11], convolutional neural network [12], [13], EMG-driven model [14], Hill-based state-space model [15]. To obtain high estimation accuracy, all of these approaches need multiple electrodes placed on different muscles to detect multi-channel sEMG. However, the use of a large number of electrodes has several limitations in practice [8]: firstly, it may be difficult to collect the sEMG signals from some specific muscles because of weakness or spasticity; secondly, the mechanical/signal interference between sEMG sensors and wearable robots/environment (e.g., sitting on a chair) also limits the

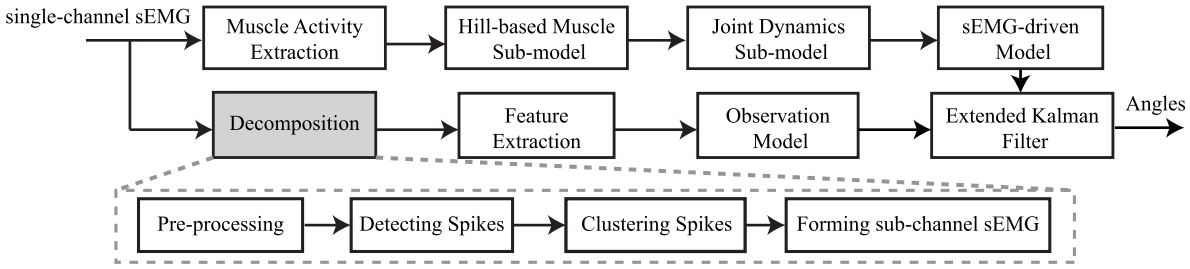

Fig. 1. Flowchart of the proposed method. The dotted box showed the flowchart of the decomposition algorithm.

acquisition of sEMG signals; thirdly, increasing the number of electrodes would increase the cost and preparation/calibration time. The above drawbacks limit the possible applications of the sEMG-based HRI in mobile and wearable robotic devices. Therefore, it is important to improve the performance of continuous movement estimation based on a minimal number of electrodes [16], [17].

Extracting more muscular information from sEMG signals effectively reduces the required number of sEMG sensors to ensure the high accuracy of human joint estimation. One of the most common methods of augmenting muscular information is decomposing sEMG signals into motor unit action potentials (MUAPs). In practice, the measured sEMG signals are influenced by many factors, such as skin and fat [18]. The amplitude and frequency of the sMEG signals are only coarse indicators of the neural-driven characteristics, which cannot fully reflect the motion information. The MUAPs propagated by the innervated muscle fibers cumulated and composed the sEMG signals, which contained more muscular information than directly measured sEMG signals [18], [19]. Several decomposition techniques have been proposed to obtain MUAPs from sEMG signals. Blind-source separation methods, including convolution kernel compensation (CKC) [20], [21], [22] and progressive FastICA peel-off (PFP) [23], have been developed to decompose high-density sEMG signals into MUAPs.

Inspired by the decomposition in high-density sEMG signals, one-channel sEMG signals can also be decomposed into m sub-channels to obtain more muscular information, although the decomposed signals can not be directly regarded as MUAPs. Meanwhile, neuromusculoskeletal modeling method can overcome the limitation of training sample scale related to the complexity of the sEMG models [24]. In this study, an sEMG-driven state-space model combined with an sEMG decomposition algorithm is proposed for guaranteeing the performance of knee-joint motion estimation from single-channel sEMG signals (see Fig. 1). The sEMG decomposition algorithm is aimed to extract more muscular information by decomposing one-channel sEMG into multiple sub-channels depending on the shape of detecting spikes. Then an observation function is designed based on features extracted from the sub-channel signals to correct the knee joint angles estimated by an sEMG-driven model in the state-space model. The single-channel sEMG signals are recorded from the gastrocnemius, which has the functions for both foot plantar flexion and knee joint flexion [25], [26]. And the sEMG signals of gastrocnemius can be easily obtained. From the practical application perspective, the proposed method can ensure more usability and robustness in knee exoskeletons for rehabilitation or performance enhancement. The contributions of this study are given as follows:

1). Developing a decomposition method depending on the shape of the sEMG signals' spikes to extract more muscular information.
2). Proposing a scheme to estimate knee joint angles from single-channel sEMG signals using an sEMG decomposition algorithm and a state-space model-based joint estimation method.
3). Evaluating the effectiveness of the proposed method to show that it can be comparable to the state-of-the-art methods with multi-channel sEMG signals.
4). Discussing the effect of the decomposed sub-channel number and walking speeds on the performance.

This work is an extended version of our previous conference publication [27](received Best Paper Award) that further includes: 1) introducing more technical details of the state-space model derivation; 2) applying a second-order dynamics model and a nonlinear transfer function to calculate the muscle activities with respect to mimic the physiological generation process of human movements; 3) using the Levenberg-Marquardt algorithm and particle swarm optimization to identify the constants in the sEMG-driven model; 4) re-designing experiments of the robustness with respect to walking speeds; 5) extensive validation of the proposed method via more experiments with eleven healthy subjects; 6) and detailed analysis of the proposed method performance compared to state-of-the-art methods.

II. Methods

A. Decomposition Algorithm

The process of decomposing single-channel sEMG signals has four steps, namely Pre-processing, Detecting spikes, Clustering spikes, and Forming sub-channel sEMG, as shown in the dotted box in Fig. 1. The details of these steps are described as follows.

1) Pre-Processing: A second-order differentiator [28] is used to filter the raw sEMG signals to remove background noise and improve the signal-to-noise ratio. This filter is defined as:

$$z_i = x_{i+2} - x_{i+1} - x_i + x_{i-1} \tag{1}$$

where x and z denote the raw sEMG signal and the pre-filtered signal, respectively. The subscript i denotes the index of sampling time.

2) Detecting Spikes: The process of detecting spikes mainly contains calculating a detection threshold and determining peak positions. The spikes are detected if the filtered signals are over the threshold. The threshold (μ) is calculated by the following equation [29]

$$\mu = 1.5\sqrt{\frac{1}{N}\sum_{i=1}^{N} z_i^2} \tag{2}$$

where N indicates the number of sample points. The parameter 1.5 is the experimental value [29].

Two baselines (with values of $\pm\mu$) are set on the pre-processed sEMG to determine peak positions. The peak position (with the maximum value) appears between two neighboring positions i and j, where the sEMG signal crosses the baselines μ from down to up or $-\mu$ from up to down. The peak position is described as follows:

$$p_{peak} = arg \max_{i<k<j} \{|z_i|, \ldots, |z_k|, \ldots, |z_j|\}. \tag{3}$$

One spike is a $2h$-dimensional real vector consisting of the sampling at the peak position, the previous $h-1$ samplings before the peak, and the next h samplings after it. In this study, parameter h is chosen as 6 [29]. The spike is described as follows:

$$\text{Spike} = \{z_{p_{peak}-h-1}, \ldots, z_{p_{peak}}, \ldots, z_{p_{peak}+h}\}. \tag{4}$$

3) Clustering Spikes: After detecting, K-means is used to classify n spike vectors into m clusters determined in advance, where m presents the sub-channel number. Firstly, m vectors are randomly selected and used as initial means in m clusters. Secondly, the others are assigned to the m clusters based on the least squares Euclidean distance. Thirdly, the mean of each cluster is recalculated. Then, the last two steps are repeated until the assignment is no longer changed. The shape of each cluster's mean is considered a template.

4) Forming Sub-Channel sEMG: Generate m zero sequences with a one-to-one correspondence of m clusters. In each sequence, the spikes from the same cluster are reordered by their positions in the original sEMG signals and are placed on this sequence. The values on other positions of this sequence are set as zero. According to this method, m sub-channel sEMG, i.e., generated m sequences, are formed.

B. State-Space Model

A state-space model consisting of an sEMG-driven model and an observation model is proposed to estimate the knee joint angle. The sEMG-driven model and observation model are established based on a Hill-based muscle sub-model [30] and the extracted features from sub-channel sEMG signals, respectively. The details are described as follows.

1) sEMG-Driven Model: The sEMG-driven model is built based on the Hill-based muscle sub-model (calculating the muscle force from EMG signals) and a joint dynamics sub-model (mapping the force to joint motion). Before that, the single-channel sEMG signals should be converted into muscle activation using a second-order dynamics model (5) and a nonlinear transfer function (6)

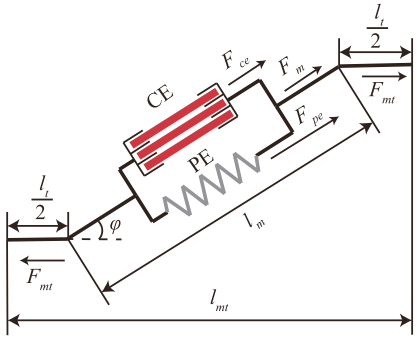

Fig. 2. Hill-based muscle sub-model. CE and PE represent the active contractile and passive elastic elements, respectively. F_{ce}, F_{pe}, F_m, and F_{mt} are the forces of the contractile element, passive elastic element, muscle fiber, and the musculotendinous unit, respectively. l_m, l_t, and l_{mt} are the length of muscle fiber, tendon, and the musculotendinous unit, respectively. ϕ represents the pennation angle.

$$u(t) = \alpha e(t-d) - \beta_1 u(t-1) - \beta_2 u(t-2) \tag{5}$$

$$a(t) = \frac{e^{Au(t)} - 1}{e^A - 1} \tag{6}$$

where $u(t)$ is neural activation; $e(t)$ is the filtered sEMG; α, β_1, and β_2 are coefficients that define the dynamics model with the constraints: $\beta_1 = \gamma_1 + \gamma_2$, $\beta_2 = \gamma_1\gamma_2$, $\alpha = 1 + \beta_1 + \beta_2$, $|\gamma_1| < 1$, and $|\gamma_2| < 1$; d is the electromechanical delay; $a(t)$ is the muscle activation; A is the nonlinear shape factor varying between -3 to 0.

On the basis of the Hill-based muscle sub-model, a muscle-tendon model is generally arranged in series with two parallel elements: an active contractile element (CE) generating active muscle force F_{ce} and a passive elastic element (PE) generating passive muscle force F_{pe}, as shown in Fig. 2.

The muscle force is the combined force of F_{ce} and F_{pe}, which calculated as follows:

$$F_{mt} = F_m \cos\phi = (F_{ce} + F_{pe})\cos\phi \tag{7}$$

where F_m denotes the force generated by muscle fibers. ϕ is the pennation angle, which is set as a constant in this study.

The F_{ce} and F_{pe} are expressed as:

$$\begin{cases} F_{ce} = f_c(l) f_c(v) a F_{\max} \\ F_{pe} = f_p(l) F_{\max} \end{cases} \tag{8}$$

where $f_c(l)$, $f_c(v)$, and $f_p(l)$ denote the active force-length relationship, the force-velocity relationship, and the passive force-length relationship, respectively. l is the normalized muscle fiber length, $l = l_m / l_m^o$, where l_m and l_m^o represent the muscle fiber length and the optimal muscle fiber length, respectively. a is the muscle activation. $F_{\max}$ is the maximum isometric muscle force, which is set as a constant in this study.

The muscle fiber length l_m can be calculated from the tendon length l_t and the musculotendinous unit length l_{mt}. According to Fig. 2, the relationship among l_m, l_{mt}, and l_t is described as:

$$l_{mt} = l_t + l_m \cos\phi. \tag{9}$$

The l_{mt} can also be expressed by a first-order polynomial of the joint angle [31]

$$l_{mt} = b_0 + b_1\theta \tag{10}$$

where b_0 and b_1 are constant values. θ is the joint angle.

Combining (9) and (10), the muscle fiber length can be expressed by joint angle θ:

$$l_t = \frac{b_0 + b_1\theta}{\cos\phi}. \tag{11}$$

Therefore, the value of F_{mt} is only related to two variables, i.e., muscle activation a and joint angle θ, since the physiological parameters ($F_{\max}, l_m^o, l_t, \phi$) are all considered as constants. In the joint dynamics sub-model, joint torque τ is calculated as follows:

$$\tau = F_{mt} r_{mt} \tag{12}$$

where r_{mt} shows the moment arm.

In [32], the moment arm can be calculated by

$$r_{mt} = \frac{\partial l_{mt}}{\partial\theta} = b_1. \tag{13}$$

According to the joint dynamics, the angular acceleration $\ddot{\theta}$ of the joint can be calculated as:

$$\ddot{\theta} = \frac{\tau - G}{I_e} = \frac{\tau - G_{\max}\sin\theta}{I_e} \tag{14}$$

where the G is the gravitational moment, and the $G_{\max}$ is the maximum value of G. I_e is the moment of inertia of the knee joint.

Substituting (7)-(13) into (14), the angular acceleration can be expressed by muscle activation and knee joint angles. The sEMG-driven model can be obtained

$$\begin{cases} \ddot{\theta}_{t+1} &= (c_0 + c_1\theta_t + c_2\theta_t^2)a(t) + c_3 e^{c_4\theta_t} - c_5\sin\theta_t \\ \dot{\theta}_{t+1} &= \dot{\theta}_t + \Delta t\ddot{\theta}_t \\ \theta_{t+1} &= \theta_t + \Delta t\dot{\theta}_t \end{cases} \tag{15}$$

where the $c_j (j = 0, 1, \ldots, 5)$ are constants identified using a Levenberg-Marquardt algorithm [33] and particle swarm optimization, which are related with physiological parameters ($F_{\max}, l_m^o, l_t, \phi$), $G_{\max}$, I_e, b_0, and b_1. $\ddot{\theta}_{t+1}$, $\dot{\theta}_{t+1}$, and θ_{t+1} denote the angular acceleration, angular velocity, and angle at time $t+1$, respectively. Δt denotes the sampling time.

2) Observation Model: An observation model is built to correct the estimated angles from the sEMG-driven model. In this study, the observation model is constructed by two kinds of sub-channel sEMG signals features, i.e., root mean square (RMS) and waveform length (WL) are used as observations, which are calculated as follows:

$$\text{RMS} = \sqrt{\frac{1}{N_w}\sum_{i=1}^{N_w}(s_i)^2} \qquad \text{WL} = \sum_{i=1}^{N_w - 1}|s_{i+1} - s_i| \tag{16}$$

where s_i denotes the ith sample of one sub-channel sEMG signals. N_w is the size of a time window calculated by the time window length divided by the sampling time of the sub-channel sEMG signals. In this work the window length is 256 ms, and the increment is 50 ms. The optimal window length was generally 200 ms and 300 ms for static contractions and dynamic contractions, respectively [34]. Thus, the delay caused by a 256 ms time window with a 50 ms increment is acceptable in real-time application.

Second-order polynomials are used as the observation functions to map the relationships between the two features and joint motions

$$h_t^{ij} = k_0^{ij} + k_1^{ij}\theta_t + k_2^{ij}\dot{\theta}_t + k_3^{ij}\theta_t^2 + k_4^{ij}\dot{\theta}_t^2 + k_5^{ij}\theta_t\dot{\theta}_t \tag{17}$$

where $i = 1, 2$, and $j = 1, 2, \ldots m$; h_t^{1j} and h_t^{2j} represent the RMS and WL features of j th sub-channel sEMG, respectively. $k_l (l = 0, 1, \ldots, 5)$ are constants that are identified using a least squares method.

Combining (15) and (17), a state-space model is built and described as follows:

$$\begin{cases} \mathbf{X}_{t+1} = \mathbf{f}(\mathbf{X}_t, a_t) + \mathbf{w}_t \\ \mathbf{Y}_{t+1} = \mathbf{h}(\mathbf{X}_{t+1}) + \mathbf{v}_t \end{cases} \tag{18}$$

where $\mathbf{X}_t = (\ddot{\theta}, \dot{\theta}, \theta)$. $\mathbf{f}(\mathbf{X}_t, a_t)$ is the sEMG-driven model, i.e., (15). $\mathbf{h}(\mathbf{X}_{t+1})$ is the observation model, i.e., (17). $\mathbf{w}_t \sim N(0, Q)$ and $\mathbf{v}_t \sim N(0, R)$ are the process noise and observation noise, respectively.

In the following, an extended Kalman filter (EKF) is applied to estimate the joint angles from (18). Define the current state vector as $\hat{\mathbf{X}}_t$ with a covariance of $\mathbf{P}_t$. The first step performs a prediction of the next state $\hat{\mathbf{X}}_{t+1|t}$ and its covariance $\mathbf{P}_{t+1|t}$ by (19)

$$\begin{cases} \hat{\mathbf{X}}_{t+1|t} = \mathbf{f}(\hat{\mathbf{X}}_t, a_t) \\ \mathbf{P}_{t+1|t} = \mathbf{F}_t\mathbf{P}_t\mathbf{F}_t^T + Q \end{cases} \tag{19}$$

where $\mathbf{F}$ is the Jacobian matrix of $\mathbf{f}(\cdot)$.

The next step corrects the predicted state and its covariance through (20)

$$\begin{cases} \mathbf{K}_{t+1} = \mathbf{P}_{t+1|t}\mathbf{H}_{t+1}^T(\mathbf{H}_{t+1}\mathbf{P}_{t+1|t}\mathbf{H}_{t+1}^T + R)^{-1} \\ \hat{\mathbf{X}}_{t+1} = \hat{\mathbf{X}}_{t+1|t} + \mathbf{K}_{t+1}(\mathbf{y}_{t+1} - \mathbf{h}(\hat{\mathbf{X}}_{t+1|t})) \\ \mathbf{P}_{t+1} = (\mathbf{I} - \mathbf{K}_{t+1}\mathbf{H}_{t+1})\mathbf{P}_{t+1|t} \end{cases} \tag{20}$$

where $\mathbf{H}$ is the Jacobian matrix of $\mathbf{h}(\cdot)$; $\mathbf{K}_{t+1}$ is the Kalman gain.

III. Experiments

A. Subjects

Eleven non-disabled subjects (six males and five females, aged 24.58 ± 3.00 years old; referenced as S1-S11) participated in the experiments. Seven subjects (S1-S7) attended the single-speed walking experiments, while the remaining four (S8-S11) participated in the multi-speed walking experiments. Referring to the results reported in [35] that the walking speed for pedestrians (aged from 14 to 65) was 1.25 m/s, we chose the gait speed of 1.25 m/s as the normal walking speed. Before the experiments, each participant was fully informed of the experimental purpose and procedures and provided their written consent to participate in this study. The experiments were approved by the local ethics committee of Nankai University, China.

B. Experimental Protocols

1) Single-Speed Experiments: In the beginning, two sEMG sensors (acquiring sEMG signals under a sample rate of 5 kHz) and two inertial measurement units (acquiring knee joint angle under a sample rate of 100 Hz) were attached to the subject's muscles (lateral gastrocnemius (LG) and medial gastrocnemius (MG)) and right lower limb (thigh and shake), respectively. All the signals were simultaneously and synchronously collected by a real-time target machine (dSPACE), as shown in Fig. 3(a). Then the sensors' outputs are calibrated when the subject is standing statically. After that, each subject was asked to perform 11 trials of walking (60 s per trial) on a treadmill at a speed of 1.25 m/s with a 3-min break in-between to avoid muscle fatigue. For each subject, data from one trial was used to calibrate the parameters of the proposed model. And data from the other trials were applied to test the method.

2) Multi-Speed Experiments: Due to the experimental setup used during the single-speed walking test was no longer available during multi-speed testing, another experimental setup with an sEMG system and a vision system was utilized, as shown in Fig. 3(b). It has been reported that both IMU measurement and markers-based motion capture measurement are capable of providing human joint kinematics [36]. The accuracies of these two experimental setups (IMU-based: 0.5 degree; vision-based: 0.2 mm) are both acceptable for evaluating the proposed method. During the multi-speed experiments, two sEMG sensors (a sample of rate 5 kHz) and 27 markers (acquiring knee joint angle under a sample of rate 100 Hz) were attached to the subject's muscles (same as the single-speed experiment) and body (16 worn on the lower limb, 8 worn on the arm, 3 worn on the trunk), respectively. A synchronization signal was applied to collect all the signals synchronously. Then, a calibration process (same as the above experiments) is performed. Each subject (S8-S11) was asked to walk on the treadmill at the speed of 0.75 m/s, 0.9 m/s, 1 m/s, 1.25 m/s, 1.35 m/s, and 1.5 m/s, respectively. Three trials were acquired under each speed. Likewise, for each subject, data from the first trial with a speed of 1.25 m/s was used to calibrate the parameters, and data from the other seventeen trials were used for testing.

C. Experimental Evaluation

For each subject, the estimated knee angles of each testing trial are separately evaluated using three criteria, i.e., normal root-mean-squared error (NRMSE), correlation coefficient (CC), and R-Square (R^2). Then, for all subjects, the evaluation results at the same speed are statistically analyzed. The three criteria are calculated as follows:

$$\mathrm{NRMSE} = \frac{\sqrt{\frac{1}{N_n}\sum_{k=1}^{N}(\theta_k - \hat{\theta}_k)^2}}{\theta_{\max} - \theta_{\min}} \tag{21}$$

$$\mathrm{CC} = \frac{C_{\theta\hat{\theta}}}{\sigma_\theta \sigma_{\hat{\theta}}} \qquad \mathrm{R}^2 = 1 - \frac{\sum_{k=1}^{N}(\theta_k - \hat{\theta}_k)^2}{\sum_{k=1}^{N}(\theta_k - \bar{\theta})^2} \tag{22}$$

where N_n denotes the sample size of one trial. θ_k and $\hat{\theta}_k$ represent the measured and the estimated knee joint angles at the sample k, respectively. $\bar{\theta}$ is the mean value of the measured angles. $\theta_{\max}$ and $\theta_{\min}$ are the maximum and minimum values of the measured knee joint angles, respectively. $C_{\theta\hat{\theta}}$ denotes the covariance between the measured and estimated angles, σ_θ and $\sigma_{\hat{\theta}}$ indicate the standard deviation of the measured and estimated angles, respectively.

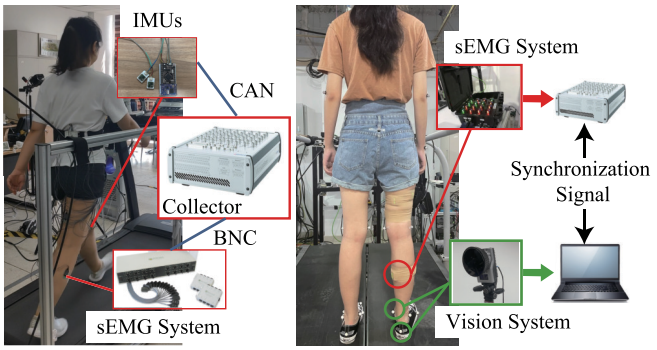

(a) (b)

Fig. 3. (a) The experimental setup for the single-speed walking test. (b) The experimental setup for the multi-speed walking test.

IV. Results

A. Decomposition Results

For each subject in the single-speed experiments, his/her single-channel sEMG signals measured from LG and MG muscles were decomposed into 2-10 sub-channels using the proposed decomposition algorithm, respectively. The decomposition results of the LG signals with 5 sub-channels from S1 were shown as representative examples (See Fig. 4). Fig. 4 (a) presented the pre-filtered sEMG signals. Fig. 4 (b) showed the spikes (the gray lines) in the same cluster. The pattern of each sub-channel, the red star line, is the mean of the detected spikes. Fig. 4 (c) presented the decomposed sub-channel sEMG signals. Based on the shape of the spikes, the single-channel sEMG signals can be decomposed into several sub-channels, which can eliminate some superposition effects. Although the sub-channel sEMG signals can not be directly considered as MUAPs, they still contain more muscular information compared to directly measured single-channel signals, which can be demonstrated in the next subsections.

B. Estimation Results

The identified parameters of the sEMG-driven model from LG and MG are given, respectively, in Tables I and II. It can be seen that the parameters among the eleven subjects are largely different, which mainly reflects that the positive and negative signs of the identified c_0, c_1, and c_2 parameters are inconsistent. The parameters should be consistent with the role of the LG or MG in knee flexion and extension physiologically, such as positive c_0, c_1, and c_2 values. But one muscle, i.e., LG or MG, replaces the multiple muscles to affect knee movement in our study. Thus, the parameters will lose the initial physiological function. Moreover, some studies demonstrated that some muscle synergies differed between individuals, which could explain the large variability of identified parameters among the eleven subjects [37], [38].

TABLE I
IDENTIFIED PARAMETERS OF THE SEMG-DRIVEN MODEL FROM LG

Subject	c_0	c_1	c_2	c_3	c_4	c_5
S1	824.89	-6210.6	-1718.1	34.04	-0.38	-0.5
S2	28.29	-183.38	-2767.4	22.38	-0.27	40.64
S3	26.84	-1000.2	-8621.3	13.2	-0.26	9.38
S4	-57.43	628.04	-2937.6	22.92	-0.32	33.57
S5	11.05	797.5	-974.53	14.87	-0.22	62.85
S6	121.73	-1765.2	-1667.8	47.65	-0.42	48.6
S7	82.34	216.52	-202.38	5.75	-0.14	60.83
S8	371.22	333.75	-100.72	12.9	-0.26	57.49
S9	790.45	1879.7	-6301.8	0.17	-14.12	60.14
S10	1021.1	5029.4	-1035.1	1.22	-11.46	53.95
S11	574.23	-2.17	-167.08	12.63	-0.24	58.14

TABLE II
IDENTIFIED PARAMETERS OF THE SEMG-DRIVEN MODEL FROM MG

Subject	c_0	c_1	c_2	c_3	c_4	c_5
S1	-246.32	757.99	-5346	35.33	-0.41	13.69
S2	-253.4	801.91	-1845.6	27.98	-0.3	54.95
S3	-109.5	-561.63	-1645.5	15.27	-0.21	51.02
S4	218.88	-2141.5	-4219	27.81	-0.32	12.4
S5	-241.19	-156.04	-1460.8	20.19	-0.21	56.43
S6	-69.8	-1691.2	71.57	60.34	-0.48	66.97
S7	102.52	194.87	-186.44	5.63	-0.14	60.97
S8	1882.7	2356.4	-3880.8	13	-0.43	38.79
S9	578.79	1737.5	-3780.4	0.28	-12.96	63.61
S10	1235.5	6860.4	-1254.5	1.25	-11.48	54.42
S11	150.67	377.25	-253.72	13.88	-0.24	59.34

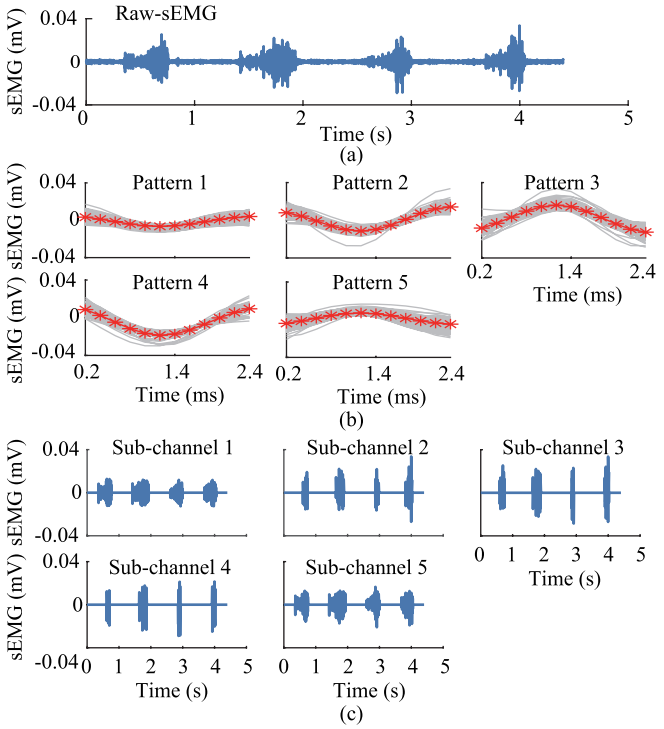

Fig. 4. Illustration of the decomposition process with decomposing the sEMG signals of LG from S1 into 5 sub-channels. (a) The pre-filtered sEMG signals. (b) The pattern of each sub-channel. (c) The decomposed sub-channel sEMG signals.

Knee joint angles of all subjects in single-speed walking experiments were estimated using the non-decomposed single-channel sEMG signals (ND-S) and the decomposed signals with m sub-channels (D-S-m, m from 2 to 10), respectively. Fig. 5 presents the results of S1 using the ND-S and D-S-5, respectively, in which the gait cycle is divided based on the shape of the knee joint angles measured by IMUs. The differences between the estimated (solid lines) and measured angles (dash lines) were obviously reduced when using the decomposed LG/MG sEMG signals compared to using the non-decomposed signals.

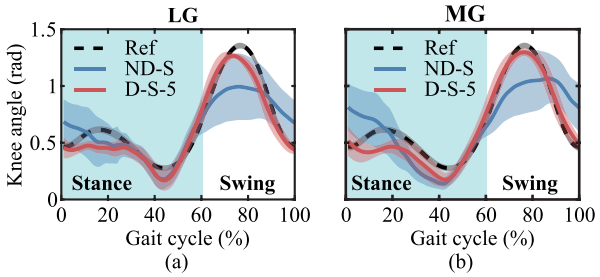

Fig. 5. Comparisons between the average measured (solid line) and estimated (dash lines) knee joint angles of S1 across 386 strides. The symbols "ND-S" and "D-S-5" represent the non-decomposed single-channel sEMG signals and decomposed sEMG signals with 5 sub-channels, respectively. (a) Estimation results from LG. (b) Estimation results from MG.

To quantitatively evaluate the estimation results between ND-S and D-S-m, three indicators mentioned above were used, and the results of all subjects are shown in Fig. 6. The detailed analyses of the results are given as follows:

1). The mean NRMSE values of D-S-m were less than or equal to 14.32±2.73% (D-S-2, LG) or 14.36±2.87% (D-S-2, MG), which were decreased by 24.15±15.62% (LG) and 27.76±23.09% (MG) compared to the ND-S (LG: 19.29±3.55%, MG: 20.83±4.38%).

2). The average CC values of D-S-m were greater than or equal to 0.902±0.039 (D-S-2, LG) or 0.904±0.027 (D-S-2, MG), which were increased by 14.63±11.24% (LG) and 27.62±32.35% (MG) compared to the ND-S (LG: 0.793±0.079, MG: 0.742±0.143).

3). In addition, the mean R^2 values of D-S-m were greater than or equal to 0.758±0.089 (D-S-2, LG) or 0.762±0.085 (D-S-2, MG), which were increased by 25.80± 21.66% (LG) and 43.66±40.44% (MG) compared to the ND-S (LG: 0.567±0.139, MG: 0.492±0.189).

To determine if the differences between the experimental results with D-S-m and ND-S were statistically significant, the Kruskal-Wallis test was conducted on the NRMSE, CC, and R^2, respectively. The statistical results showed that all $p-$values were smaller than 0.05, as shown in Fig. 6. These results suggested that the estimation accuracy using D-S-m significantly outperformed that using ND-S. The results demonstrated that the proposed state-space model with the decomposition algorithm can effectively improve the estimation accuracy.

C. Influence of Sub-Channel Number

It is also interesting to study the effects of sub-channel number on knee angle estimation accuracy. Fig. 7 presented the relationship between the estimation accuracy and the sub-channel number across all subjects in the single-speed experiments. When the sub-channel number was below 3, the

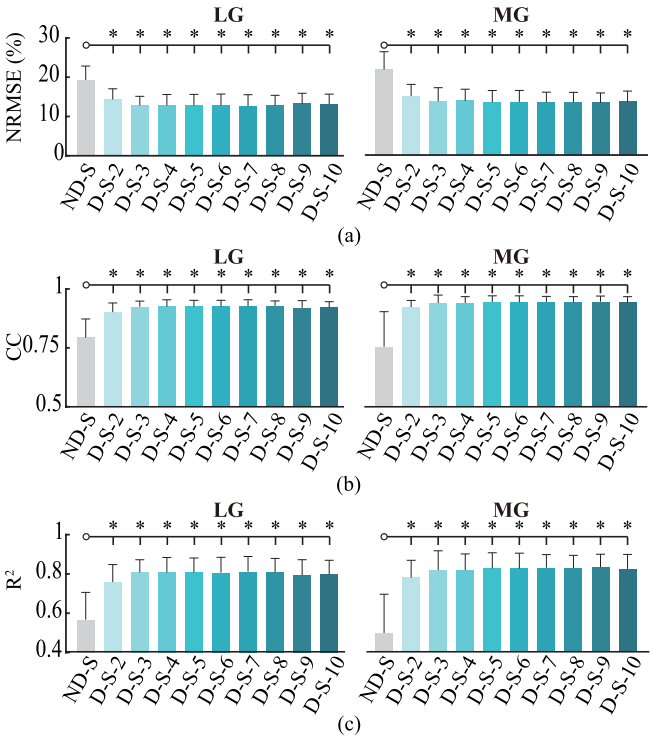

Fig. 6. Comparison estimation accuracy of different sub-channel sEMG signals. (a) NRMSE values; (b) CC values; (b) R^2 values. ND-S: non-decomposed single-channel sEMG signals; D-S-*m*: decomposed sEMG signals with *m* sub-channels, *m* from 2 to 10. The left and right of each subfigure present the results of single-channel sEMG from LG and MG, respectively. Bars and whiskers are means and standard deviations across all subjects in the single-speed experiments. *Statistical significance ($p < 0.05$) with respect to ND-S.

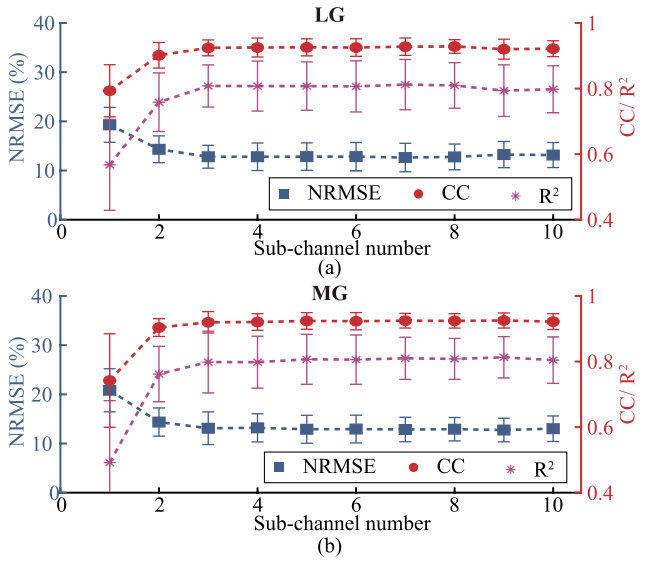

Fig. 7. The relationship between the estimation accuracy and the sub-channel number across all subjects in the single-speed experiments. Left ordinate: NRMSE values; Right ordinate: CC and R^2 values; Abscissa: the sub-channel number. (a) The accuracy with single-channel sEMG signals from LG. (b) The accuracy with single-channel sEMG signals from MG.

TABLE III
STATISTICAL RESULTS BETWEEN D-S-3 AND OTHER D-S-*m* ACROSS ALL SUBJECTS IN THE SINGLE-SPEED EXPERIMENTS

No.	D-S-3					
	LG			MG		
	NRMSE	CC	R^2	NRMSE	CC	R^2
2	**0.0068**	**0.0000**	**0.0084**	**0.0225**	**0.0047**	**0.0108**
4	0.8813	0.6484	0.9005	0.5498	0.8556	0.4826
5	0.9775	0.5317	0.8753	0.9689	0.6121	0.8914
6	0.9968	0.7560	0.9839	0.9378	0.7699	0.9896
7	0.6896	0.3597	0.6718	0.9741	0.6490	0.9896
8	0.9069	0.3910	0.9261	0.7699	0.7898	0.8505
9	0.3472	0.6369	0.3513	0.9741	0.6821	0.8454
10	0.4267	0.6311	0.5804	0.6917	0.9223	0.8658

No. presents the decomposed sub-channel number.
The bold denotes the statistical significance with respect to D-S-3.

NRMSE values decreased significantly along with the sub-channel number, and the values of CC and R^2 increased significantly along with the sub-channel number. The estimation accuracy remained high and stable when the number was over 3. The Kruskal-Wallis test was also used to determine if there were differences between the D-S-3 and the other D-S-*m* ($m = 2, 4, 5, 6, 7, 8, 9, 10$). Table III showed the $p-$values on NRMSE, CC, and R^2. Statistical differences in all the evaluation criteria were found between D-S-2 and D-S-3 ($p < 0.05$). No differences were found between D-S-3 and the other D-S-*m* ($m = 4, 5, 6, 7, 8, 9, 10$). The above results demonstrated that the optimal decomposed number of LG and MG was 3 in terms of estimation accuracy and cost of computation. Some possible physiological reasons for the optimal decomposed number are discussion in the next section.

D. Influence of Walking Speeds

To verify the robustness of the proposed method to walking speeds, four subjects (S8-S11) conducted the multi-speed walking experiments. For each subject, the model established at 1.25 m/s was directly tested on six walking conditions without any calibration, including speeds of 0.75, 0.9, 1.0, 1.25, 1.35, and 1.5 m/s. Fig. 8 shows the results of a representative subject (S9), in which the gait cycle is divided based on the vertical ground reaction force measured using the treadmill. All the estimation profiles were close to the reference angle profiles. Moreover, the average values of the evaluation criteria from the four subjects were listed in Table IV. The results indicated that the proposed method is robust with respect to walking speed covering from 0.9 m/s to 1.35 m/s with the mean NRMSE value lower than 16%, the average CC values near 0.89, and the R^2 value over 0.7. It should be noted that the NRMSE values at 0.75 m/s and 1.5 m/s are larger than the values at walking speed covering from 0.9 m/s to 1.35 m/s. Although increased NRMSE values when the walking speed is too fast or slow, relatively high CC values can be ensured. Some possible reasons are discussed in the next Section, and will be investigated in our future work.

E. Comparison Between Different Models

A recursive artificial neural network (RANN) was used to map the relationship between the muscle activation, angle, and angular velocity at time k and the angle and angular velocity at time $k + 1$. The RANN model contained four layers: one input layer, two hidden layers, and one output layer. The hidden layers had eight and four neurons, respectively. The estimation accuracy from the RANN model was compared

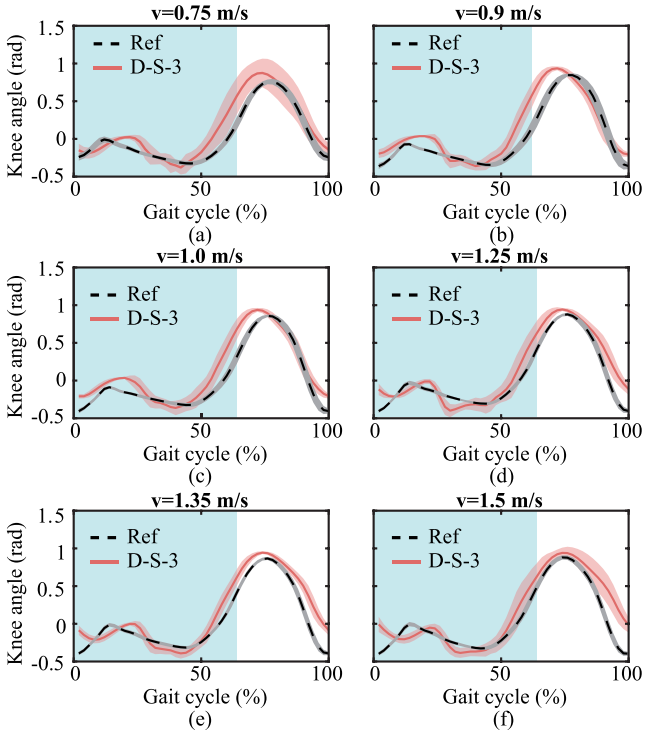

Fig. 8. Demonstration of knee angle estimation from S9 with single-channel sEMG signals of GL in multi-speed experiments.

TABLE IV
NRMSE (MEAN±STD), CC (MEAN±STD), AND R^2 (MEAN±STD) ACROSS S8-S11 USING THE DECOMPOSED SIGNALS WITH 3 SUB-CHANNELS IN MULTI-SPEED EXPERIMENTS

Speed (m/s)	NRMSE (%)	CC	R^2
0.75	20.27 ± 16.29	0.84 ± 0.14	0.62 ± 0.29
0.9	15.99 ± 3.71	0.88 ± 0.06	0.72 ± 0.13
1.0	12.97 ± 2.99	0.91 ± 0.04	0.81 ± 0.09
1.25	12.58 ± 2.69	0.92 ± 0.03	0.82 ± 0.07
1.35	14.33 ± 6.38	0.89 ± 0.06	0.77 ± 0.10
1.5	18.29 ± 3.80	0.83 ± 0.07	0.55 ± 0.24

with that of the sEMG-driven model in multi-speed experiments. The comparison results showed that the estimation accuracy by sEMG-driven model was superior to that of the RANN model when the walking speed was below 1.25 m/s, see Fig. 9. However, when the walking speed was over 1.35 m/s, the estimation performance of sEMG-driven model decreased larger than that of the RANN model. These results indicated that the two models exhibit different robustness with respect to different walking speeds.

V. DISCUSSION

In this study, a method namely the sEMG-driven state-space model combined with an sEMG decomposition algorithm is proposed to provide a reference trajectory to enhance voluntary participation, which is important for control of rehabilitation robots (e.g., [39], [40], [41]). Meanwhile, single-channel sEMG replaced the multiple-channel sEMG in this study, which can largely reduce the calibration time and improve the wearer's comfort. Moreover, muscle synergy is a widely accepted hypothesis to understand muscle coordination [42], [43]. It has been postulated that the central nervous system

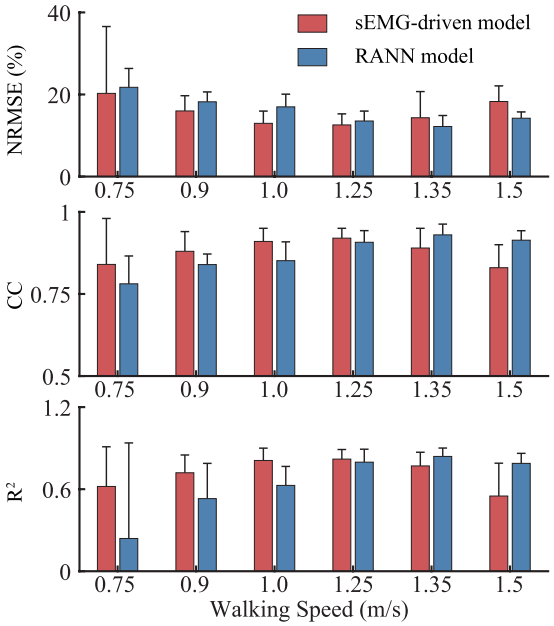

Fig. 9. Comparison estimation accuracy between different models in the multi-speed experiments.

controls muscles in groups during functional tasks. The results of this study indicated that the knee joint angles can be accurately estimated based on the single-channel sEMG of gastrocnemius, which gives a good agreement with the muscle synergy.

The activity of gastrocnemius is a strong correlation with the knee joint angles during walking. This is the physiological reason that the knee joint angles can be accurately estimated based on the single-channel sEMG of gastrocnemius using the proposed method. A determining factor in adapting the proposed method to the other joints is whether there is a strongly correlated muscle with the motion of these joints. Therefore, it is possible to generalize this method to other joints, such as the hip joint or elbow joint. For example, hip joint angles may be accurately estimated from single-channel sEMG signals of vastus using this method. When this method is applied to the other joints, the model of the joint dynamics should be carefully established, considering whether external loads of the joint exist.

It is observed that three sub-channels was the optimal decomposed number of LG and MG (see Fig. 7 and Table IV). From the physiological perspective, the three decomposed sub-channel sEMG signals may be related to three kinds of neurons in gastrocnemius, including Type S units, Type FR units, and Type FF units, as shown in a prior study [44]. When the sub-channel number was over three, the sEMG signals maight be just decomposed meticulously from the these three types. It is a possible reason that the estimation accuracy cannot be improved significantly with sub-channel number over three. Although it is impossible to have the one-to-one correspondence between the three types and the three sub-channel sEMG signals, it does not affect its advantage in the motion estimation, which can effectively increase the estimation accuracy.

The proposed state-space model with the decomposed sub-channel sEMG signals can be robustness to different

TABLE V
COMPARISON WITH RELATED RESEARCH

Ref	Number of channels	Walking speed (km/h)	Methods	Performance knee angle
[48]	10	2.88, 3.6, 4.32	Deep belief networks	CC = 0.97±0.04
[49]	8	3, 3.5, 4	Multi-branch neural network	CC = 0.96±0.03 R^2 = 0.91±0.07
[50]	8	0.5, 1.0, 2.0, 3.0	Synergy-based deep learning	R^2 = 0.87±0.029
[51]	8	2.0, 2.5, 3.0, 3.5	Muscle synergy-driven ANFIS model	CC = 0.92±0.05 R^2 = 0.84±0.01
This work	**1**	2.7, 3.24, 3.6, 4.5, 4.86, 5.4	Decomposition-based state-space model	CC = 0.92±0.03 R^2 = 0.82±0.07

walking speeds. The main reason may be that the Hill-based muscle sub-model and the joint dynamics sub-model incorporates the anatomical and biomechanical structures/constraints of the lower limb's neuromusculoskeletal system. The state-space model can well mimic the physiological generation process of human movements by explicitly representing the anatomical and biomechanical structures/constraints [45].

Although a few studies attempted to use single-channel sEMG signals to perform the classification of lower limb movement modes or the estimation of upper limb muscle force [46], [47], to the best of our knowledge, this is the first study to use single-channel sEMG signals to estimate the knee joint angles. Therefore, we only compared the proposed method to the existing ones using multi-channel sEMG signals for knee joint movement estimation. It showed that the performance of the proposed method (using sEMG of gastrocnemius with three sub-channels) was comparable to those of the state-of-the-art studies using multi-channel sEMG signals (see Table V). It should be noted that the proposed method is firstly established with a small dataset measured only one walking speed and tested with a wide range of walking speeds from 0.75 m/s to 1.5 m/s (covering the main walking speed range of healthy adult subjects) while the studies like [48], [49], and [51] utilized the training data covering all experimental speeds to train their models. Therefore, the proposed method has application potential for individuals with neurological diseases whose sEMG signals from some specific muscles were collected with difficulty. Moreover, it has significant potential for various applications of gait patterns, such as level-ground walking, stair-ascent, and ramp-ascent because the muscle synergy phenomenon can also be observed during such activities. We will further evaluate the performance of the method during different daily living activities in future work.

Walking speeds significantly affected gait patterns with respect to joint kinematics, joint kinetics, and ground reaction force [52]. As walking speeds increase, not only does the muscle activation of gastrocnemius increase, but also the periods of peak muscle activation change in the whole gait cycle. The change of the knee angle magnitude is significantly lower compared to the change of the muscle activation in a wide range of walking speeds. The inconsistent changes between the muscle activation and knee angles are considered as the main reason that leads to large estimation errors. A possible way to further enhance the performance of the proposed method for these speeds is to consider change rules of muscle activation and knee joint angles with walking speeds in the EMG-driven model when modeling. In future work, we will further design experimental protocol and recruit more subjects to study such change rules.

VI. CONCLUSION AND FUTURE WORK

This study focused on improving the accuracy of human joint angle estimation using single-channel sEMG signals to overcome the limitations in robust practical applications, such as weakness or spasticity of one or more specific muscles, mechanical/signal interference between the sEMG sensors and wearable robots/environment, or discomfort during long-term routine use. For this purpose, a novel method, which includes a decomposition algorithm and a state-space model, was proposed. The proposed method was evaluated with eleven healthy subjects to estimate the knee joint angles using LG or MG sEMG signals. The experimental results indicated this method has significant potential benefits over multi-channel sEMG-based methods for joint angle estimation with mobile and wearable robotic devices in practice.

In future work, we will study the change rule between the muscle activation and the knee angle with different walking speeds, and evaluate the proposed method with more subjects, including older and disabled subjects, and under more practical scenarios such as stair-ascent, ramp-ascent, and level-ground walking.

REFERENCES

[1] TWC of the Report, "Report on cardiovascular health and diseases in China 2021: An updated summary," *Biomed. Environ. Sci.*, vol. 35, no. 7, pp. 573–603, 2022.

[2] J. S. Lora-Millan, F. J. Sanchez-Cuesta, J. P. Romero, J. C. Moreno, and E. Rocon, "A unilateral robotic knee exoskeleton to assess the role of natural gait assistance in hemiparetic patients," *J. NeuroEng. Rehabil.*, vol. 19, no. 1, pp. 1–24, Oct. 2022.

[3] B. Chen, B. Zi, Z. Wang, L. Qin, and W.-H. Liao, "Knee exoskeletons for gait rehabilitation and human performance augmentation: A state-of-the-art," *Mechanism Mach. Theory*, vol. 134, pp. 499–511, Apr. 2019.

[4] M. K. Shepherd and E. J. Rouse, "Design and validation of a torque-controllable knee exoskeleton for sit-to-stand assistance," *IEEE/ASME Trans. Mechatronics*, vol. 22, no. 4, pp. 1695–1704, Aug. 2017.

[5] W. Huo, S. Mohammed, and Y. Amirat, "Impedance reduction control of a knee joint human-exoskeleton system," *IEEE Trans. Control Syst. Technol.*, vol. 27, no. 6, pp. 2541–2556, Nov. 2019.

[6] D. Xiong, D. Zhang, X. Zhao, and Y. Zhao, "Deep learning for EMG-based human–machine interaction: A review," *IEEE/CAA J. Autom. Sinica*, vol. 8, no. 3, pp. 512–533, Mar. 2021.

[7] E. Zheng, J. Wan, L. Yang, Q. Wang, and H. Qiao, "Wrist angle estimation with a musculoskeletal model driven by electrical impedance tomography signals," *IEEE Robot. Autom. Lett.*, vol. 6, no. 2, pp. 2186–2193, Apr. 2021.

[8] J. He, X. Sheng, X. Zhu, C. Jiang, and N. Jiang, "Spatial information enhances myoelectric control performance with only two channels," *IEEE Trans. Ind. Informat.*, vol. 15, no. 2, pp. 1226–1233, Feb. 2019.

[9] C. Caulcrick, W. Huo, W. Hoult, and R. Vaidyanathan, "Human joint torque modelling with MMG and EMG during lower limb human-exoskeleton interaction," *IEEE Robot. Autom. Lett.*, vol. 6, no. 4, pp. 7185–7192, Oct. 2021.

[10] C. Caulcrick, W. Huo, E. Franco, S. Mohammed, W. Hoult, and R. Vaidyanathan, "Model predictive control for human-centred lower limb robotic assistance," *IEEE Trans. Med. Robot. Bionics*, vol. 3, no. 4, pp. 980–991, Nov. 2021.

[11] F. Zhang et al., "SEMG-based continuous estimation of joint angles of human legs by using BP neural network," *Neurocomputing*, vol. 78, no. 1, pp. 139–148, Feb. 2012.

[12] C. Ma et al., "A bi-directional LSTM network for estimating continuous upper limb movement from surface electromyography," *IEEE Robot. Autom. Lett.*, vol. 6, no. 4, pp. 7217–7224, Oct. 2021.

[13] Y. Geng et al., "A CNN-attention network for continuous estimation of finger kinematics from surface electromyography," *IEEE Robot. Autom. Lett.*, vol. 7, no. 3, pp. 6297–6304, Jul. 2022.

[14] J. W. L. Pau, S. S. Q. Xie, and A. J. Pullan, "Neuromuscular interfacing: Establishing an EMG-driven model for the human elbow joint," *IEEE Trans. Biomed. Eng.*, vol. 59, no. 9, pp. 2586–2593, Sep. 2012.

[15] Q. Ding, J. Han, and X. Zhao, "Continuous estimation of human multi-joint angles from sEMG using a state-space model," *IEEE Trans. Neural Syst. Rehabil. Eng.*, vol. 25, no. 9, pp. 1518–1528, Sep. 2017.

[16] D. Farina et al., "The extraction of neural information from the surface EMG for the control of upper-limb prostheses: Emerging avenues and challenges," *IEEE Trans. Neural Syst. Rehabil. Eng.*, vol. 22, no. 4, pp. 797–809, Jul. 2014.

[17] J. Liu, X. Sheng, D. Zhang, N. Jiang, and X. Zhu, "Towards zero retraining for myoelectric control based on common model component analysis," *IEEE Trans. Neural Syst. Rehabil. Eng.*, vol. 24, no. 4, pp. 444–454, Apr. 2016.

[18] R. Merletti and D. Farina, "Muscle coordination, motor synergies, and primitives from surface EMG," in *Surface Electromyography: Physiology, Engineering, and Applications*. Piscataway, NJ, USA: IEEE, 2016, pp. 158–179.

[19] C. J. De Luca, A. Adam, R. Wotiz, L. D. Gilmore, and S. H. Nawab, "Decomposition of surface EMG signals," *J. Neurophysiol.*, vol. 96, no. 3, pp. 1646–1657, Sep. 2006.

[20] D. Farina et al., "Noninvasive, accurate assessment of the behavior of representative populations of motor units in targeted reinnervated muscles," *IEEE Trans. Neural Syst. Rehabil. Eng.*, vol. 22, no. 4, pp. 810–819, Jul. 2014.

[21] Y. Ning, X. Zhu, S. Zhu, and Y. Zhang, "Surface EMG decomposition based on K-means clustering and convolution kernel compensation," *IEEE J. Biomed. Health Informat.*, vol. 19, no. 2, pp. 471–477, Mar. 2015.

[22] C. Chen, G. Chai, W. Guo, X. Sheng, D. Farina, and X. Zhu, "Prediction of finger kinematics from discharge timings of motor units: Implications for intuitive control of myoelectric prostheses," *J. Neural Eng.*, vol. 16, no. 2, Apr. 2019, Art. no. 026005.

[23] M. Chen, X. Zhang, X. Chen, and P. Zhou, "Automatic implementation of progressive FastICA peel-off for high density surface EMG decomposition," *IEEE Trans. Neural Syst. Rehabil. Eng.*, vol. 26, no. 1, pp. 144–152, Jan. 2018.

[24] W. Wang et al., "Prediction of human voluntary torques based on collaborative neuromusculoskeletal modeling and adaptive learning," *IEEE Trans. Ind. Electron.*, vol. 68, no. 6, pp. 5217–5226, Jun. 2021.

[25] J. B. Morrison, "The mechanics of the knee joint in relation to normal walking," *J. Biomech.*, vol. 3, no. 1, pp. 51–61, Jan. 1970.

[26] L. Li, D. Landin, J. Grodesky, and J. Myers, "The function of gastrocnemius as a knee flexor at selected knee and ankle angles," *J. Electromyogr. Kinesiol.*, vol. 12, no. 5, pp. 385–390, Oct. 2002.

[27] S. Zhang, J. Zhang, and J. Han, "Continuous estimation of knee angles from decomposition of single channel surface electromyography signals," in *Proc. 27th Int. Conf. Mechatronics Mach. Vis. Pract. (M2VIP)*, Shanghai, China, Nov. 2021, pp. 446–451.

[28] K. C. McGill, K. L. Cummins, and L. J. Dorfman, "Automatic decomposition of the clinical electromyogram," *IEEE Trans. Biomed. Eng.*, vol. BME-32, no. 7, pp. 470–477, Jul. 1985.

[29] D. W. Stashuk, "Decomposition and quantitative analysis of clinical electromyographic signals," *Med. Eng. Phys.*, vol. 21, nos. 6–7, pp. 389–404, Jul. 1999.

[30] T. S. Buchanan, D. G. Lloyd, K. Manal, and T. F. Besier, "Neuromusculoskeletal modeling: Estimation of muscle forces and joint moments and movements from measurements of neural command," *J. Appl. Biomech.*, vol. 20, no. 4, pp. 367–395, Nov. 2004.

[31] J. J. Visser, J. E. Hoogkamer, M. F. Bobbert, and P. A. Huijing, "Length and moment arm of human leg muscles as a function of knee and hip-joint angles," *Eur. J. Appl. Physiol. Occupational Physiol.*, vol. 61, nos. 5–6, pp. 453–460, Dec. 1990.

[32] F. E. Zajac, "Muscle and tendon: Properties, models, scaling, and application to biomechanics and motor control," *Crit. Rev. Biomed. Eng.*, vol. 17, no. 4, pp. 359–411, 1989.

[33] D. W. Marquardt, "An algorithm for least-squares estimation of nonlinear parameters," *J. Soc. Ind. Appl. Math.*, vol. 11, no. 2, pp. 431–441, Jun. 1963.

[34] F. D. Farf, J. C. Politti, and C. J. Felice, "Evaluation of EMG processing techniques using information theory," *BioMed. Eng. OnLine*, vol. 9, p. 72, Dec. 2010.

[35] R. L. Knoblauch, M. T. Pietrucha, and M. Nitzburg, "Field studies of pedestrian walking speed and start-up time," *Transp. Res. Rec., J. Transp. Res. Board*, vol. 1538, no. 1, pp. 27–38, Jan. 1996.

[36] S. Tadano, R. Takeda, and H. Miyagawa, "Three dimensional gait analysis using wearable acceleration and gyro sensors based on quaternion calculations," *Sensors*, vol. 13, no. 7, pp. 9321–9343, Jul. 2013.

[37] W. van den Hoorn, P. W. Hodges, J. H. van Dieën, and F. Hug, "Effect of acute noxious stimulation to the leg or back on muscle synergies during walking," *J. Neurophysiol.*, vol. 113, no. 1, pp. 244–254, Jan. 2015.

[38] F. Hug and K. Tucker, "Muscle coordination and the development of musculoskeletal disorders," *Exercise Sport Sci. Rev.*, vol. 45, no. 4, pp. 201–208, Oct. 2017.

[39] W. Hassani, S. S. Mohammed, and Y. Y. Amirat, "Real-time EMG driven lower limb actuated orthosis for assistance as needed movement strategy," in *Proc. RSS*, 2013, pp. 1–9.

[40] T. Lenzi, S. M. M. De Rossi, N. Vitiello, and M. C. Carrozza, "Intention-based EMG control for powered exoskeletons," *IEEE Trans. Biomed. Eng.*, vol. 59, no. 8, pp. 2180–2190, Aug. 2012.

[41] G. Durandau, W. F. Rampeltshammer, H. van der Kooij, and M. Sartori, "Neuromechanical model-based adaptive control of bilateral ankle exoskeletons: Biological joint torque and electromyogram reduction across walking conditions," *IEEE Trans. Robot.*, vol. 38, no. 3, pp. 1380–1394, Jun. 2022.

[42] J. Taborri et al., "Feasibility of muscle synergy outcomes in clinics, robotics, and sports: A systematic review," *Appl. Bionics Biomech.*, vol. 2018, pp. 1–19, Nov. 2018.

[43] N. A. Alibeji, V. Molazadeh, F. Moore-Clingenpeel, and N. Sharma, "A muscle synergy-inspired control design to coordinate functional electrical stimulation and a powered exoskeleton: Artificial generation of synergies to reduce input dimensionality," *IEEE Control Syst. Mag.*, vol. 38, no. 6, pp. 35–60, Dec. 2018.

[44] R. A. Garnett, M. J. O'Donovan, J. A. Stephens, and A. Taylor, "Motor unit organization of human medial gastrocnemius," *J. Physiol.*, vol. 287, no. 1, pp. 33–43, Feb. 1979.

[45] N. Jiang et al., "Bio-robotics research for non-invasive myoelectric neural interfaces for upper-limb prosthetic control: A 10-year perspective review," *Nat. Sci. Rev.*, vol. 10, no. 5, Apr. 2023, Art. no. nwad048.

[46] C. Wei et al., "Single-channel surface electromyography signal classification with variational mode decomposition and entropy feature for lower limb movements recognition," *Biomed. Signal Process. Control*, vol. 74, Apr. 2022, Art. no. 103487.

[47] W. Sun, J. Zhu, Y. Jiang, H. Yokoi, and Q. Huang, "One-channel surface electromyography decomposition for muscle force estimation," *Frontiers Neurorobot.*, vol. 12, p. 20, May 2018.

[48] J. Chen, X. Zhang, Y. Cheng, and N. Xi, "Surface EMG based continuous estimation of human lower limb joint angles by using deep belief networks," *Biomed. Signal Process. Control*, vol. 40, pp. 335–342, Feb. 2018.

[49] X. Wang et al., "SEMG-based consecutive estimation of human lower limb movement by using multi-branch neural network," *Biomed. Signal Process. Control*, vol. 68, Jul. 2021, Art. no. 102781.

[50] D. Xiong, D. Zhang, X. Zhao, Y. Chu, and Y. Zhao, "Synergy-based neural interface for human gait tracking with deep learning," *IEEE Trans. Neural Syst. Rehabil. Eng.*, vol. 29, pp. 2271–2280, 2021.

[51] W. Zhong, X. Fu, and M. Zhang, "A muscle synergy-driven ANFIS approach to predict continuous knee joint movement," *IEEE Trans. Fuzzy Syst.*, vol. 30, no. 6, pp. 1553–1563, Jun. 2022.

[52] C. A. Fukuchi, R. K. Fukuchi, and M. Duarte, "Effects of walking speed on gait biomechanics in healthy participants: A systematic review and meta-analysis," *Syst. Rev.*, vol. 8, p. 153, Jan. 2019.